Computational Mechanics 28 (2002) 390–400 © Springer-Verlag 2002
DOI 10.1007/s00466-002-0303-5

Meshless method for modeling of human proximal femur: treatment of nonconvex boundaries and stress analysis

K. M. Liew, H. Y. Wu, T. Y. Ng

Abstract In this paper, a meshless method based on the kernel particle approximation is employed for the simulation of the human proximal femur. The proposed formulation considers treatments of nonconvex boundaries and material discontinuities in the bone structure. A preprocessor is developed for the generation of the discretized scatter particles model. Application examples were employed to explore certain stress distribution phenomena in the human proximal femur with consideration for the detrimental effects of infarction as well as aging. The effects of stress variations were also examined exposing some very interesting biomechanical features.

Keywords Meshless method, Reproducing kernel particle approximate, Nonconvex boundary, Proximal femur, Biomechanics

1 Introduction

The use of numerical methods has become commonplace in biomechanics over the past two decades. As compared to experimental techniques, numerical methods often prove to be the more economical choice, besides offering the possibility of investigating locations not accessible to experimental devices. Historically, the finite element method (FEM) has been used, almost exclusively, for stress analysis in biomechanics (Huiskes and Chao 1983). For biomechanical problems in orthopaedic biomechanics, bone remodeling, implantation and joint replacement, a stress analysis is an absolute necessity, by which the data of stress distribution and stress values at particular locations of interest are obtained.

Several authors, including Hansen and Koeneman (1987) and Weinans (1991), have employed three-dimensional finite element models for orthopaedic biomechanics analyses. The use of three-dimensional models is, however, labor and computationally intensive, and simplified two-dimensional analyses should always be considered first. In a number of cases, relevant information on stress distributions in biomechanical structures can also be obtained with less effort by a two-dimensional analysis (Vander Sloten et al. 1993). Hedia et al. (1996) reviewed the two-dimensional FEM models that have been used by many researchers in the stress analysis of femoral component in the context of total hip replacement. Generally, a two-dimensional FEM model is much more economical in terms of computational effort and is easier to incorporate within an optimization algorithm than a three-dimensional analysis (Yang et al. 1984). However, there are various assumptions, which must be made in order to reduce the actual three-dimensional geometry to an equivalent two-dimensional model. Brown et al. (1982) use two-dimensional (plane-strain) stress fields to evaluate femoral head load transmission changes occurring with infarction as well as normal growth. An equivalent two-dimensional plane stress model was also employed by Hedia et al. (1996), to examine the effects of FEM idealization, load conditions and interface assumptions, on the stress distribution in the human femur with an endoprosthesis. The validity of the two-dimensional FEM model of a femur was discussed in detail by Hayes and Snyder (1981).

The boundary element method (BEM) has also been employed for bone remodeling analysis by Sadegh et al. (1993). In the above mesh-based methods, great efforts have to be made to deal with the complex geometries, with problems associated with mesh distortion and mesh refinement or remeshing becoming inevitable.

In recent time, meshless methods have attracted significant attention in computational mechanics research. The element-free Galerkin method (EFG) and reproducing kernel particle method (RKPM) are the most popular meshless techniques suitable for structural analysis. The EFG method based on the moving least-squares method is advanced by Belytschko et al. (1994) and the RKPM using integral transformation with a corrected kernel function was presented by Liu et al. (1994, 1995). Li et al. (2000) used the RKPM for the simulation of large deformation of thin shell structures. The RKPM was also employed for modeling of large deformation analysis by Liew et al. (2002a). A meshfree solution method which has integrated the RKPM with parametric quadratic programming was formulated by Liew et al. (2002b) for elasto-plasticity analysis. In order to investigate the dynamic behaviour of rotating shells, Liew et al. (2002c) has proposed the

Received 20 January 2001 / Accepted 30 May 2001

K. M. Liew (✉), H. Y. Wu
Nanyang Centre for Supercomputing and Visualisation,
School of Mechanical and Production Engineering,
Nanyang Technological University,
Nanyang Avenue, Singapore 639798
e-mail: mkmliew@ntu.edu.sg

T. Y. Ng
Institute of High Performance Computing,
89 C Science Park Drive, #02, 11/12,
The Rutherford, Singapore 118261

harmonic reproducing kernel particle (HRKP) method. They showed that this HRKP method has produced excellent results for this problem.

In this study, a meshless method based on the kernel particle method for the human proximal femur stress analysis is presented. Nonconvex boundary problems and bimaterial interface discontinuities are considered. By using the meshless approach, domains of interest are discretized only by a scattered set of particles, uncumbered by elements and elemental connectivity. This avoids problems associated with mesh distortion and does away with the possible need for remeshing. Numerical examples are considered for the human proximal femur, femur with infarct and various age effects. Comparisons with FEM (ANSYS) results show that the present meshless method is an effective numerical tool for the simulation of the present biomechanics application.

2
Review of reproducing kernel particle method

In the smooth particle hydrodynamics or SPH approach, an approximation $u^k(x)$ to $u(x)$ in a domain Ω is generated by a kernel approximation given by

$$u^k(x) = \int_\Omega \phi_a(x-y)u(y)\mathrm{d}y \tag{1}$$

Liu et al. (1995a, b) proposed a reproducing kernel approximation by introducing a correction function to the SPH kernel estimate of Eq. (1) as

$$u^R(x) = \int_\Omega C(x;x-y)\phi_a(x-y)u(y)\mathrm{d}y \tag{2}$$

where $u^R(x)$ is the "reproduced function" of $u(x)$. Equation (2) is called the reproducing equation, and $C(x;x-y)$ is the correction function defined by

$$C(x;x-y) = \sum_{i=0}^{N} b_i(x)(x-y)^i = b^T(x)H(x-y) \tag{3}$$

where $H^T(x-y) = [1, x-y, \ldots, (x-y)^N]$ and $b^T(x) = [b_0(x), b_1(x), \ldots, b_N(x)]$ are determined by imposing the N-th order polynomial. The reproducing kernel approximation is

$$\begin{aligned} u^R(x) &= \int_\Omega C(x;x-y)\phi_a(x-y)u(y)\mathrm{d}y \\ &= H^T(0)M^{-1}(x)\int_\Omega H(x-y)\phi_a(x-y)u(y)\mathrm{d}y \end{aligned} \tag{4}$$

Equation (4) can be recast into the following form

$$u^R(x) = \int_\Omega \bar{\phi}_a(x;x-y)u(y)\mathrm{d}y \tag{5}$$

where $\bar{\phi}_a(x;x-y) = C(x;x-y)\phi_a(x-y)$ is the reproduced kernel. Since Eq. (4) exactly reproduces an N-th order polynomial, this method fulfills the N-th order consistency conditions, i.e.,

$$\int_\Omega \bar{\phi}_a(x;x-y)y^n\mathrm{d}y = x^n \quad \text{for } n = 0, \ldots, N \tag{6}$$

The kernel estimate (*KE*) used in the SPH and the reproducing kernel (*RK*) approximation employed in the RKPM can be combined into the following generalized approximation equation

$$u^h(x) = \int_\Omega C(x;x-y)\phi_a(x;x-y)u(y)\mathrm{d}y \tag{7}$$

$$C(x;x-y) = \begin{cases} 1 & KE \\ H^T(0)M^{-1}(x)H(x-y) & RK \end{cases} \tag{8}$$

where $u^h(x)$ is the approximation of $u(x)$. For the purpose of utilizing the shape function for discrete approximation, discretization of Eq. (7) is required. Suppose the domain Ω is discretized by a set of particles $\{x_1, \ldots, x_{NP}\}$, where x_I is the location of the particle I, and NP is the total number of particles, then by the use of a simple trapezoidal rule, Eq. (7) can be discretized into

$$u^h(x) = \sum_{\mathrm{I}=1}^{NP} C(x;x-x_\mathrm{I})\phi_a(x-x_\mathrm{I})d_\mathrm{I}\Delta x_\mathrm{I} \tag{9}$$

$$M(x)b(x) = H(0) \tag{10}$$

The correction function $C(x;x-x_\mathrm{I})$ was determined previously from the completeness requirement of the continuous reproducing equation. With the discretization of the reproducing equation, we re-impose the completeness requirement on Eq. (10) to obtain

$$C(x;x-x_\mathrm{I}) = H^T(0)M^{-1}(x)H(x-x_\mathrm{I}) \tag{11}$$

$$M(x) = \sum_{\mathrm{I}=1}^{NP} H(x-x_\mathrm{I})H^T(x-x_\mathrm{I})\phi_a(x-x_\mathrm{I}) \tag{12}$$

$$H^T(x-x_\mathrm{I}) = [1, x-x_\mathrm{I}, \ldots, (x-x_\mathrm{I})^N] \tag{13}$$

Equation (9) can thus be expressed in the following form

$$u^h(x) = \sum_{\mathrm{I}=1}^{NP} \phi_\mathrm{I}(x)d_\mathrm{I} \tag{14}$$

$$\phi_\mathrm{I}(x) = C(x;x-x_\mathrm{I})\phi_a(x-x_\mathrm{I}) \tag{15}$$

3
Treatments of nonconvex boundaries

Biomechanical problems are essentially very geometry-based, viz., have very complicated geometries and many nonconvex boundaries. Treatment of nonconvex boundaries is one of the vital aspects for the application of meshless methods to the field of biomechanics. Organ et al. (1996) introduced the diffraction method to construct continuous and smooth approximations near nonconvex boundaries in the element-free Galerkin method (EFG). In this paper, a diffraction method according to the angle-change is used to construct continuous approximation with the presence of the nonconvex boundaries or discontinuities. In this approach, one employs a rectangular support and the determination

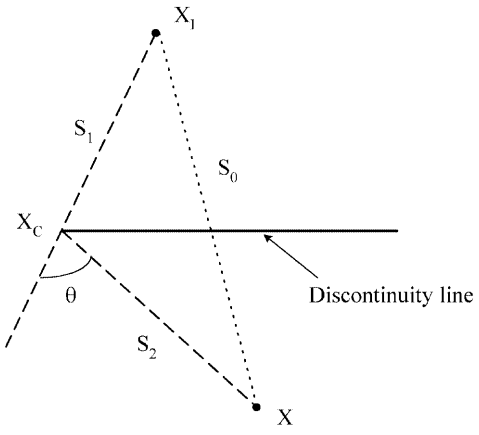

Fig. 1. Scheme of the angle-change method for determining the domain of influence

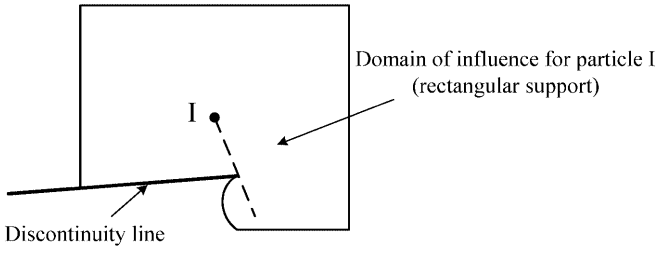

Fig. 2. The domains of influence for particle I near a line of discontinuity using the angle-change criterion

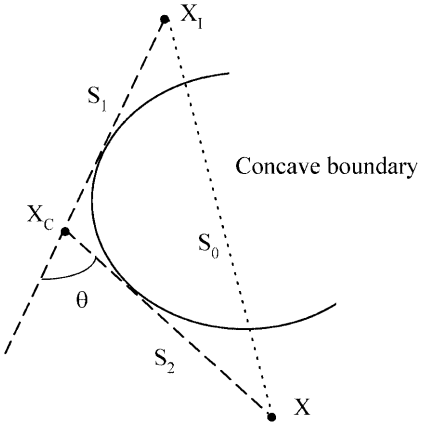

Fig. 3. Nonconvex boundaries near a concave curve

variable is angle change. Consider an evaluation point A, which may fall into the range of the particle I's rectangular support, but cannot be seen from particle I for the influence of the discontinuity line. The discontinuity may be the crack line or the other non-convex boundary, as shown in Figs. 1, 2 and 3, respectively. A coefficient is defined by

$$\wp = \begin{cases} 1 & \text{if } x \text{ is visible from } x_I \\ 1/\cos(\theta) & \text{if } x \text{ isinvisible from } x_I \end{cases} \quad (16)$$

It can be proven that (see Figs. 1 and 2) if the following equation holds,

$$\cos(\theta) = \frac{s_0^2 - (s_1^2 + s_2^2)}{2s_1 s_2} \quad (17)$$

then the kernel function parameter d_{xI} and d_{yI} are defined as

$$dx_I = |x - x_I| \cdot \wp, \quad dy_I = |y - y_I| \cdot \wp \quad (18)$$

when θ is very small and $\wp$ approaches unity. These points will still lie within the support of particle I. However when θ is near 90°, $\wp$ becomes very large and reaches maximum value. Therefore a upper bound is needed. For example, an upper bound value of 0.1 is set for $\cos(\theta)$. In case of that $\cos(\theta)$ is greater than 0.1, $\wp$ will not be computed, i.e., points outside the support of particle I will not be considered. The domain of influence of particle I is shown in Fig. 2.

4
Treatment of material discontinuity

For problems with multiple materials, the derivatives of the displacements may be, by the very nature of the problem, discontinuous across the material interfaces although the displacement continuity may exist in a piecewise manner. It is intended to consider different material regions in the modeling of proximal femur in connection with simulation of infarction. Hence, treatment of material discontinuity becomes an important modeling aspect discussed in this section. Cordes and Moran (1996) have treated discontinuous derivatives in EFG by a Lagrange multiplier technique. In this study, the Lagrange multiplier technique is taken to treat the material discontinuity in kernel particle method.

4.1
Governing equations

To demonstrate the treatment of material discontinuity in the meshless method, we consider small displacement linear elastostatics. For simplicity, the explanation will focus on two distinguishable materials separated by a single interface, Γ_s, as shown in Fig. 4. This interface is defined by n_j^-, the unit outward normal of Ω^-, along the material boundary. The governing equilibrium equation is given by

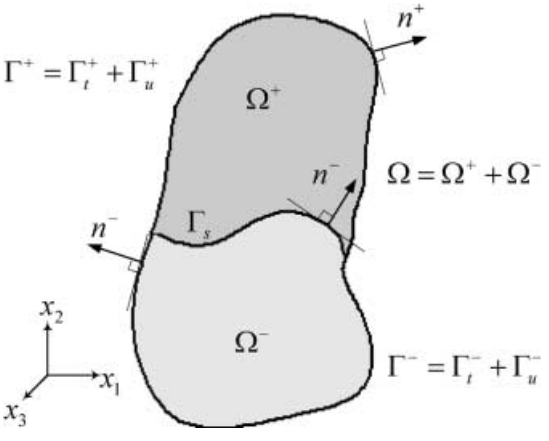

Fig. 4. A general three-dimensional inhomogeneous body

$$\sigma_{ji,j} + b_i = 0 \quad \text{in} \quad \Omega \tag{19}$$

where σ_{ij} is the Cauchy stress tensor and b_i is a body force. The associated boundary conditions are given as follows:

$$\sigma_{ij} n_j = \bar{t}_i \quad \text{on} \quad \Gamma_t \tag{20}$$

$$u_i = \bar{u}_i \quad \text{on} \quad \Gamma_u \tag{21}$$

where t_i is defined as the traction on a surface, and u_i is the displacement field. The superposed bar denotes the prescribed traction and displacement values, respectively, and n_j is the unit outward normal to the domain Ω. Due to Cauchy's relation,

$$t_i = \sigma_{ij} n_j \quad \text{on} \quad \Gamma \ , \tag{22}$$

Eq. (20) may be rewritten as

$$t_i = \bar{t}_i \quad \text{on} \quad \Gamma_t \tag{23}$$

On the interface, Γ_s, continuity of tractions and displacements requires

$$[|t_i|] = 0 \tag{24}$$

$$[|u_i|] = 0 \tag{25}$$

where [| |] denotes a jump. Equations (24) and (25) may also be interpreted as

$$t_i^+ - t_i^- = 0 \tag{26}$$

$$u_i^+ - u_i^- = 0 \tag{27}$$

Using the relationship presented in Eq. (22), the tractions in Eq. (26) are therefore defined as

$$t_i^+ = +\sigma_{ij}^+ n_j^- \tag{28}$$

$$t_i^- = +\sigma_{ij}^- n_j^- \tag{29}$$

The linear elastic constitutive relationship is given by

$$\sigma_{ij} = C_{ijkl} \varepsilon_{kl} \tag{30}$$

where C_{ijkl} is the elastic modulus, and the strain tensor, ε_{kl}, is defined as

$$\varepsilon_{kl} = \tfrac{1}{2}(u_{k,l} + u_{l,k}) \tag{31}$$

4.2
Modifications for material discontinuity

For material discontinuities, the interface constraint given by Eq. (25) must be enforced explicitly along the interface Γ_s,

$$\int_{\Gamma_s} \left(u_i^+ - u_i^-\right) \mathrm{d}\Gamma = 0 \tag{32}$$

where u_i^+ and u_i^- correspond to the displacement fields in Ω^+ and Ω^-, respectively. By imposing this constraint on the variational level, the traction continuity constraint, Eq. (24), will be weakly satisfied. To illustrate this, consider the following weak form associated with Eq. (19), where $u(x) \in H^1$ are trial functions

$$\int_\Omega \delta u_{i,j} \sigma_{ij} \, \mathrm{d}\Omega - \int_\Omega \delta u_i b_i \, \mathrm{d}\Omega - \int_{\Gamma_t} \delta u_i \bar{t}_i \, \mathrm{d}\Gamma - \int_{\Gamma_s} \delta \gamma_i \left(u_i^+ - u_i^-\right) \mathrm{d}\Gamma - \int_{\Gamma_s} \left(\delta u_i^+ - \delta u_i^-\right) \gamma_i \, \mathrm{d}\Gamma = 0 \tag{33}$$

The Lagrange multipliers, γ_i, enforce the displacement continuity constraint on Γ_s. The associated Euler equations are thus

$$\sigma_{ji,j} + b_i = 0, \quad \text{in } \Omega^+ \text{ and } \Omega^- \ , \tag{34}$$

$$t_i - \bar{t}_i = 0, \quad \text{on } \Gamma_{t+} \text{ and } \Gamma_{t-} \ , \tag{35}$$

$$u_i^+ - u_i^- = 0, \quad \text{on } \Gamma_s \ , \tag{36}$$

$$\gamma_i + t_i^- = 0, \quad \text{on } \Gamma_s \ , \tag{37}$$

$$\gamma_i + t_i^+ = 0, \quad \text{on } \Gamma_s \ , \tag{38}$$

which corresponds to satisfying the equilibrium equation, Eq. (19), in both Ω^+ and Ω^-; and the traction equation, Eq. (20), on both Γ^+ and Γ^-; with the corresponding physical interpretation of the Lagrange multipliers, $\gamma_i = -t_i^- = -t_i^+$, where positive and negative superscripts refer to variables belonging to Ω^+ and Ω^-, respectively. Note that t_i^- and t_i^+ are defined according to Eqs. (28) and (29). Therefore, traction continuity at the interface (Eq. (24)) is satisfied by eliminating γ_i from Eqs. (37) and (38). The displacement continuity constraint, Eq. (25), explicitly enforced, also appears as an Euler equation given by Eq. (36). Substituting Eq. (37) into Eq. (33) yields the following modified variational form

$$\int_\Omega \delta u_{i,j} \sigma_{ij} \, \mathrm{d}\Omega - \int_\Omega \delta u_i b_i \, \mathrm{d}\Omega - \int_{\Gamma_t} \delta u_i \bar{t}_i \, \mathrm{d}\Gamma - \int_{\Gamma_s} \delta t_i^- \left(u_i^+ - u_i^-\right) \mathrm{d}\Gamma + \int_{\Gamma_s} \left(\delta u_i^+ - \delta u_i^-\right) t_i^- \, \mathrm{d}\Gamma = 0 \tag{39}$$

Discretizing the above equation leads to the following system of equations

$$Ku = f \tag{40}$$

where the matrices K and f are defined as

$$K_{IJ} = \int_\Omega B_I^T D B_J \, \mathrm{d}\Omega + \int_{\Gamma_s} \left(\phi_I^+ - \phi_I^-\right) N^- D^- B_J^- \, \mathrm{d}\Gamma + \int_{\Gamma_s} \left(B_I^-\right)^T (D^-)^T (N^-)^T \left(\phi_J^+ - \phi_J^-\right) \mathrm{d}\Gamma \tag{41}$$

$$f_I = \int_{\Gamma_t} \phi_I \bar{t} \, \mathrm{d}\Gamma + \int_\Omega \phi_I b \, \mathrm{d}\Omega + \int_{\Gamma_s} \left(\phi_I^+ - \phi_I^-\right) N^- D^- \, \mathrm{d}\Gamma \tag{42}$$

and

$$D = D_0 \begin{bmatrix} 1 & v_0 & 0 \\ v_0 & 1 & 0 \\ 0 & 0 & \frac{1-v_0}{2} \end{bmatrix} \tag{43}$$

where $D_0 = E_0/(1 - v_0^2)$, and

$$B_I = \begin{bmatrix} \phi_{I,x} & 0 \\ 0 & \phi_{I,y} \\ \phi_{I,Y} & \phi_{I,x} \end{bmatrix} \tag{44}$$

$$N = \begin{bmatrix} n_x & 0 & n_y \\ 0 & n_y & n_x \end{bmatrix} \tag{45}$$

where n_x and n_y are the component of the surface normal and the matrices B^-, D^-, and N^- in the integrals on Γ_s arise from the substitution of $\gamma_i = -t_i^-$, or the traction at the interface of Ω^- and the unit normal, N, of Γ_s. For plane stress, $E_0 = E$, $v_0 = v$; and for plane strain, $E_0 = E/(1 - v^2)$, $v_0 = v/(1 - v)$.

5
Applications of meshless method for human proximal femur stress analysis

To handle the geometrical complexities, a preprocessor is developed by integrating the well-developed geometric modeler software with the meshless solver. Using this preprocessor, the meshless modeling which includes the modeling of the geometry domain, the discretization of the interest by particles, the generation of the integration grids and the predefinition of the loads, namely the displacement constraints and forces, becomes quite convenient.

5.1
Femur (assuming homogeneous material) stress analysis

A two-dimensional plane stress meshless method is employed for the simulation of a coronal midsection of the adult proximal femur. The loading conditions are characterized as a single-legged stance, which consist of the concentrated articular contact force (the resultant force of the weight loading transferred though the articular joint), abductor muscle (gluteus medius) traction at the greater trochanter and zero displacement across a horizontal section just distal to the lesser trochanter as shown in Fig. 5. Most previous studies predicted resultant joint forces in the range of zero to four times the body weight. The geometrical data for the proximal femur is taken from open literature (Brown et al. 1982).

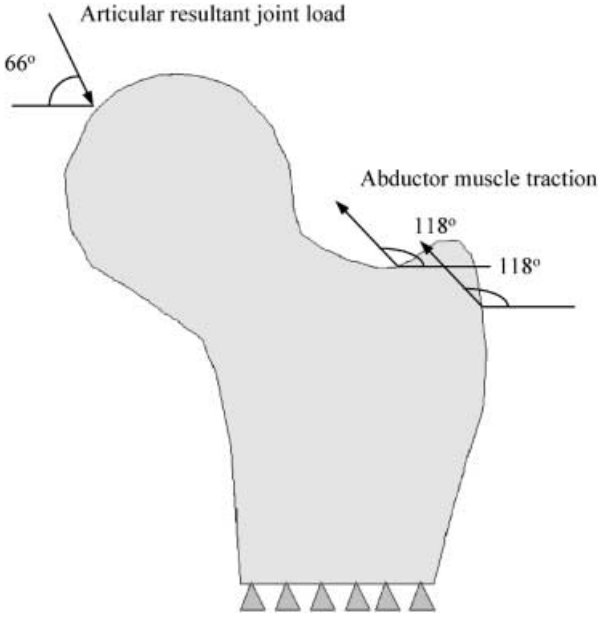

Fig. 5. Geometry, boundary condition and loading conditions for a human proximal femur model

The idealized elastic, homogeneous, isotopic femur is studied here using three different particle models, as shown in Fig. 6a, b and c. The stress values and distributions along the sections of interest, i.e., the load resultant line (L1–L2) and line L3–L4 near the femur neck, shown in Fig. 7, are examined in detail. The convergence for the line L1–L2 is given in Fig. 9 and the contour stress distribution is shown in Fig. 10. The stress magnitudes and distributions in lines L1–L2 and L3–L4 are given in Figs. 11 and

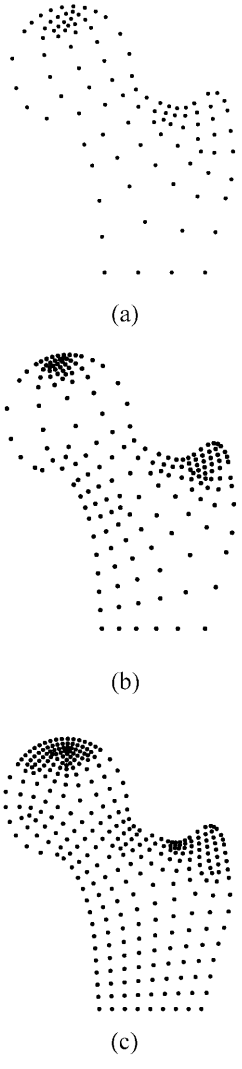

Fig. 6. Meshless analysis models – particle display: **a** particle model I, 101 particles; **b** particle model II, 180 particles; **c** particle model III, 316 particles

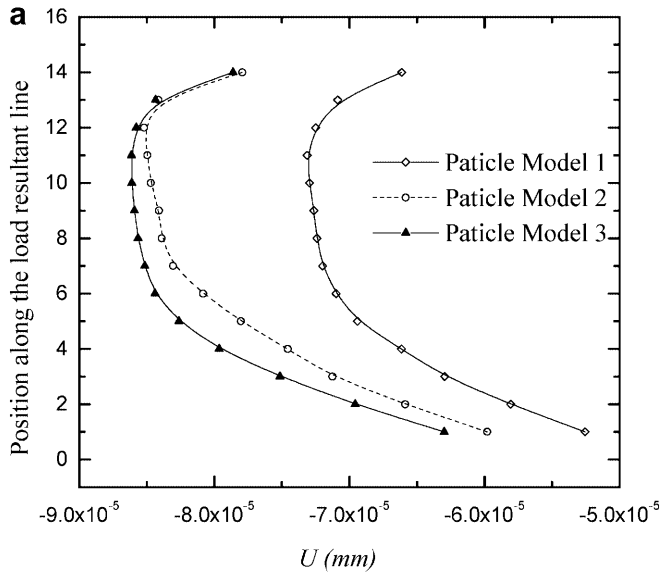

Fig. 9. Displacement values (in line L1–L2) given by three meshless models: **a** *X* direction displacement; **b** *Y* direction displacement

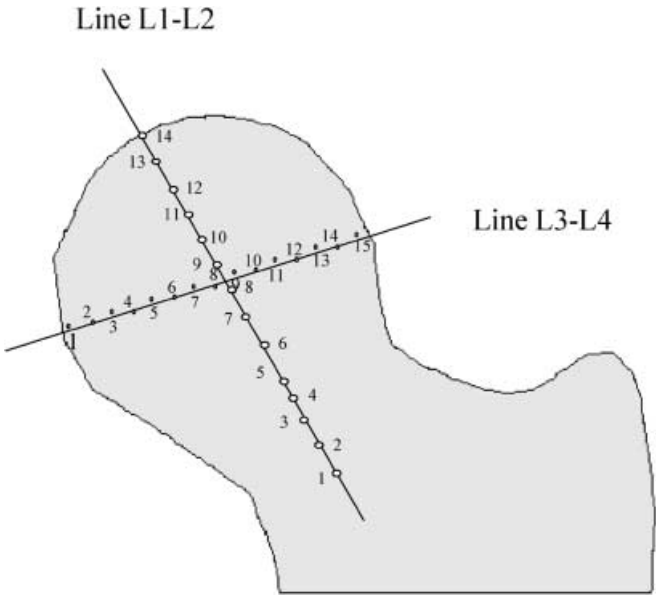

Fig. 7. Positions of line L1–L2 (the load resultant line) and line L3–L4

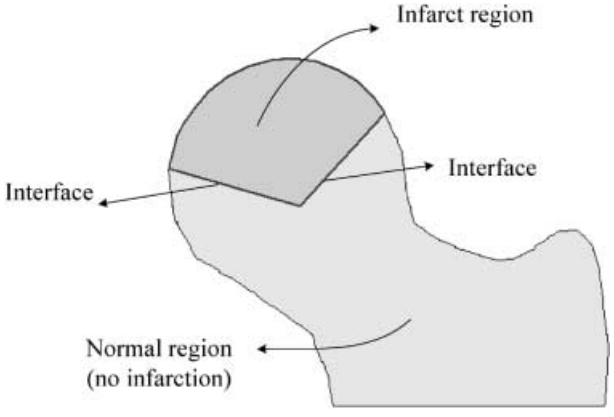

Fig. 8. Proximal femur with infarct region

12, respectively. Comparison of the stress results between meshless methods and FEM (ANSYS) are also displayed in Figs. 11 and 12. They are obviously in very good agreement and we can reasonably conclude that the present meshless methodology is an effective tool for orthopaedic biomechanics simulation.

5.2
Stress analysis of femur with infarct

To evaluate the infarct effects on the proximal femur, a standard infarct femur model, seen as two separate

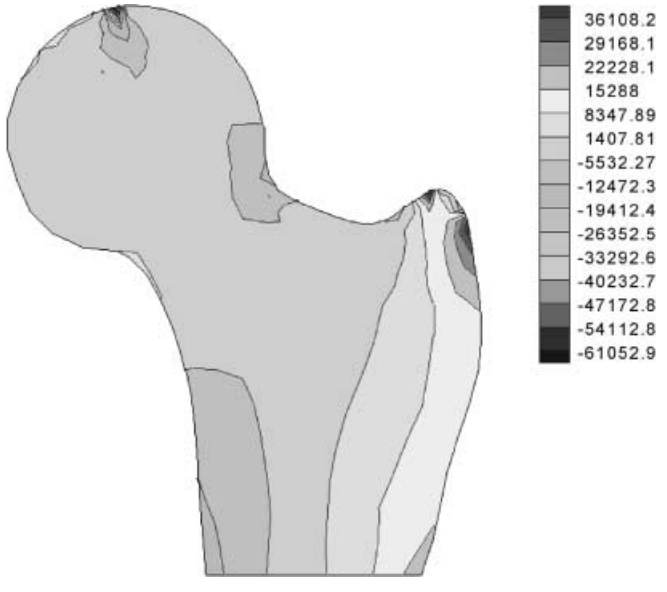

Fig. 10. Stress σ_y, distribution contours for human proximal femur

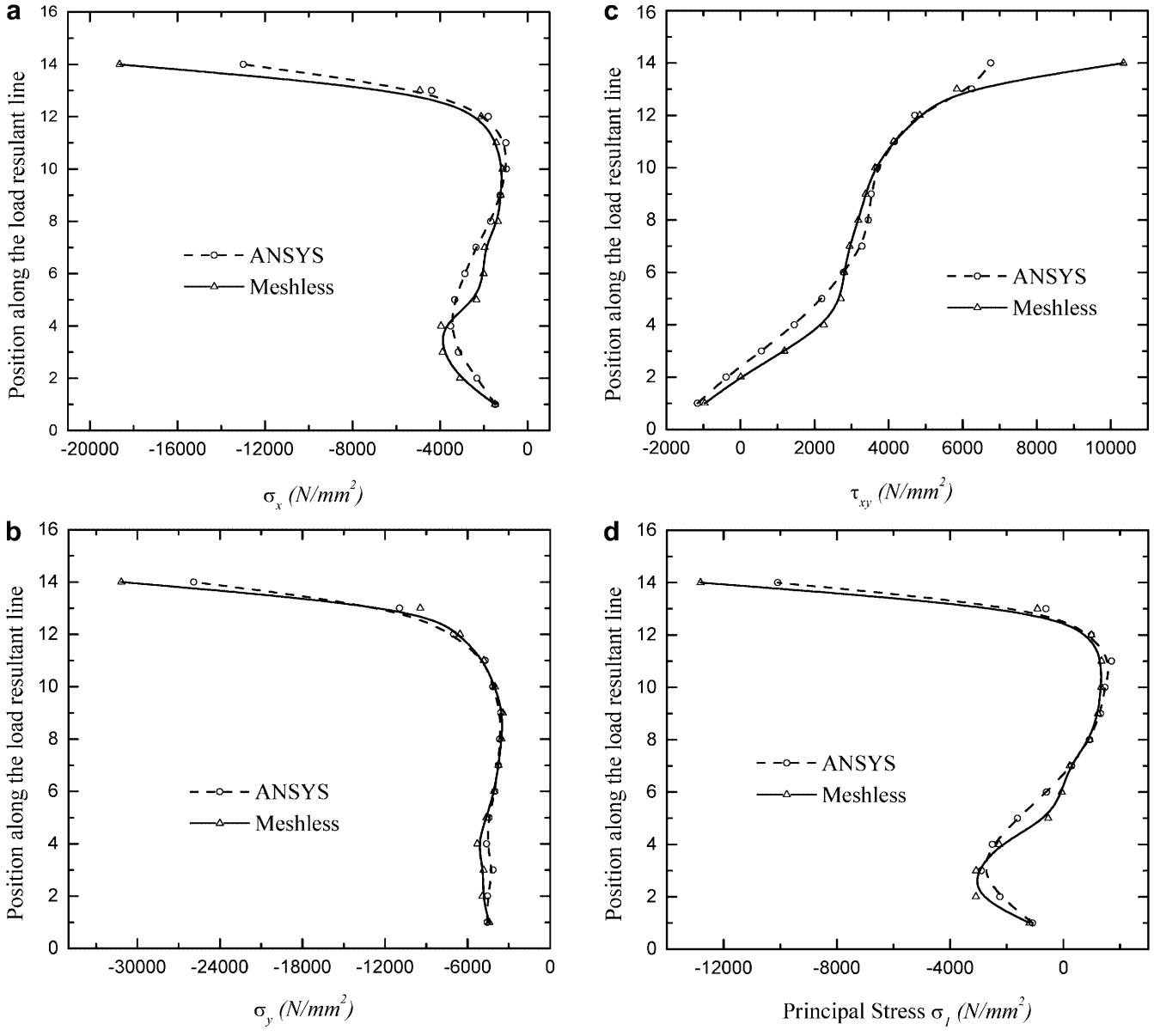

Fig. 11. Stress distribution along the load resultant line: **a** normal stress σ_x; **b** normal stress σ_y; **c** shear stress τ_{xy}; **d** principal stress σ_1

material regions, see Fig. 8, is used. The above-mentioned approach to deal with the material discontinuity and interface is employed. To study the effects of infarction, modulus values for all particles within the infarct segment are reduced to a specified fraction, C_N, of the value of the normal healthy case. In this study, C_N values ranging from 1.0 (normal healthy case) to 0.1 (very severe deficit) are considered. The longitudinal and principal stress distributions are given in Fig. 13a and b, respectively. From Fig. 13, we can see that the salient load transfer mechanisms remain operative while general reductions in stress levels within the infarct region were observed. The load transmission aberrations associated with progressively increasing infarct stiffness deficits are also shown in Fig. 13a and b. Along the line of joint load resultant, longitudinal stresses in the healthy femoral head progressively increase from the medial to under the articular surface. Progressively increasing stiffness deficits, (i.e., reductions in C_N) in the infarct, cause progressive reductions in the stress magnitude, their effect being most pronounced (for this particular lesion geometry) at about probe position 2, see Fig. 13. Examination of the principal stress along the load resultant line reveals that stiffness deficit-related stress relief experienced by the infarct's core is rapidly diminished toward the infarct periphery. The computational results nevertheless indicate a clear tendency for stress transfer from necrotic to neighboring viable regions. In general, infracted bone in the superior weight-bearing region must continue to carry near-physiological stress even though load is progressively transferred out through the distal

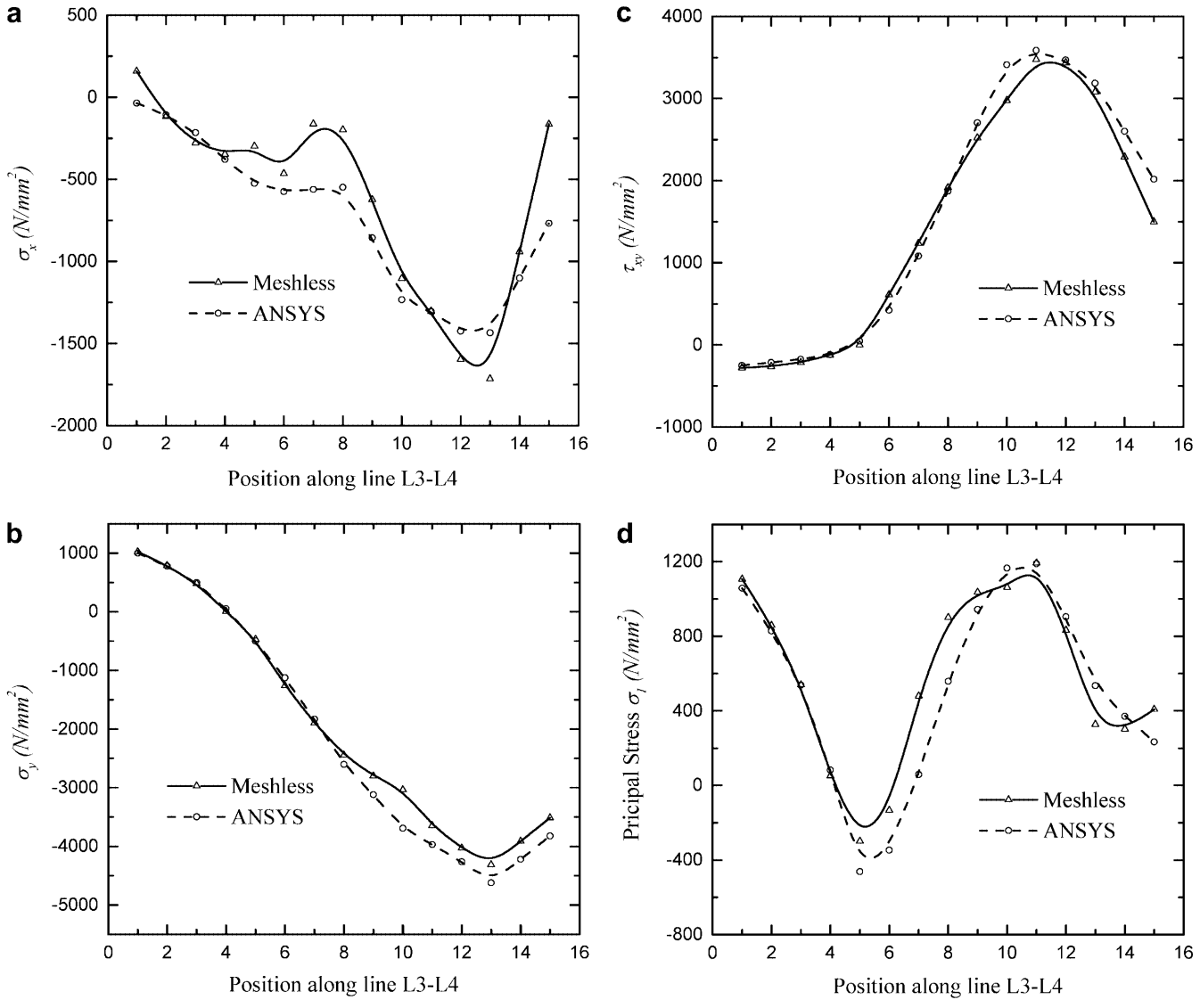

Fig. 12. Stress distribution along line L3–L4: **a** normal stress σ_x; **b** normal stress σ_y; **c** shear stress τ_{xy}; **d** principal stress σ_1

lesion periphery. Hence, vulnerability to mechanical overload would appear to be more pronounced superiorly than inferiorly. It would thus make very good sense to the surgeon planning an osteotomy to provide stress relief for necrotic regions to place greater emphasis on repositioning all or most of the superior aspect of the lesion to a new location outside the weight-bearing tract.

5.3
Stress changes with growth in the normal juvenile proximal femur

Mechanical stress is widely recognized as a major stimulus in the development and growth of bone. Biomechanical changes at the human proximal femur during growth do not result simply from increases in bone stiffness, stature and body weight, rather, profound morphological changes are at work as well. The femoral neck undergoes large relative lengthening, and the neck-shaft angle progressively decreases from nearly 180° in infancy to about 130–160° at maturity. Here we have attempted to quantify the salient load transmission changes accompanying the complex morphological alterations of growth, cases of ages one, three, seven and 18 (adult), were examined. The meshless plane-stress particle model described in Sect. 5.1 was considered a good representative model of the geometrical characteristics and the applied external loading and support conditions of the juvenile and adult proximal femur. Geometrical data for ages one, three, seven and 18 were taken from Brown et al. (1982). To introduce the effects of increase of bone stiffness during bone growth, elastic modulus values for bones of different ages were reduced to a specified age-attention fraction, C_A, of the value of adult bone. For ages one, three and seven, C_A is taken to be 0.07, 0.37 and 0.79, respectively.

Age-related variations of principal stress field for ages one, three, seven and 18 in the overall load transmission pattern are given in Fig. 14. From Fig. 14 the following major qualitative features in the stress distribution can be seen for all of these ages:

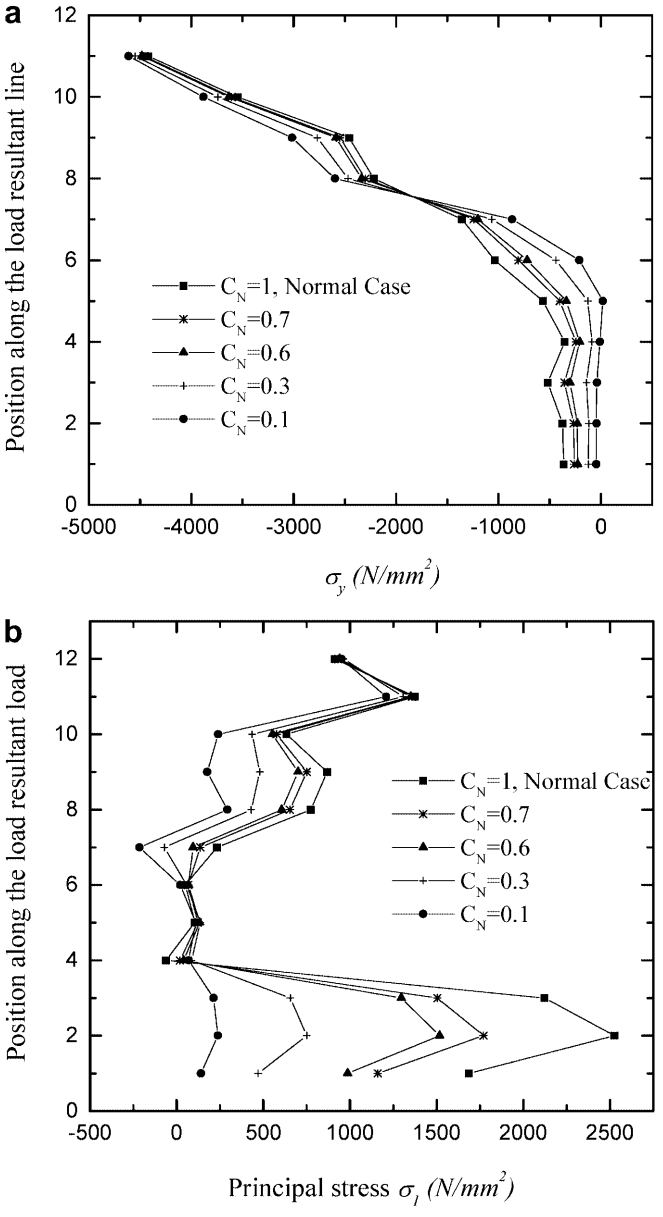

Fig. 13. The effects of infarct on longitudinal stress and principal stress along the load resultant line: **a** longitudinal stress; **b** principal stress σ_1

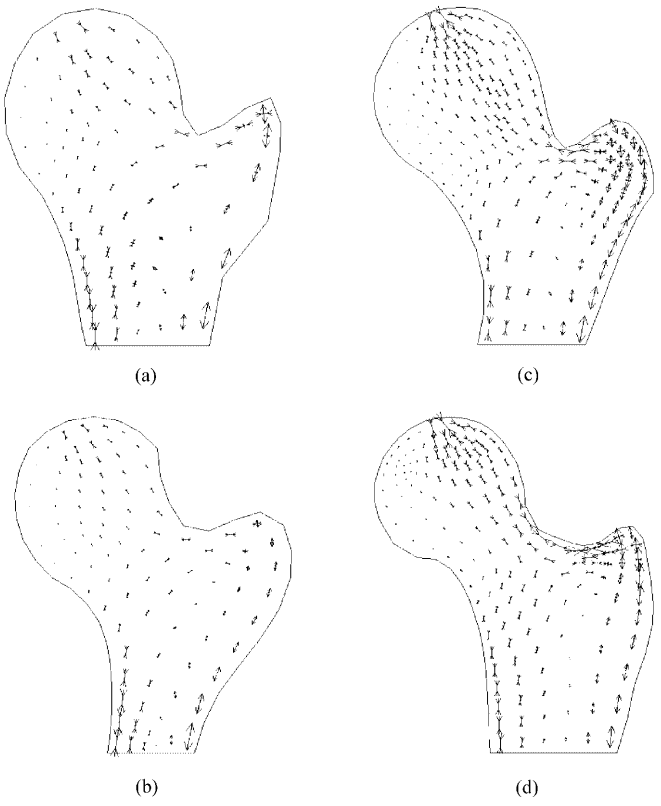

Fig. 14. Principal stress fields in the femur for: **a** age one; **b** age three; **c** age seven and **d** age 18

1. Preferential load transmission through the center of the femoral head and progressive concentration of the compressive stress along the joint load resultant line, through the medial cortex, to surface of the femoral head;
2. Strong longitudinal compressive stress along the medial cortex;
3. Low stress level in the medullary cavity;
4. Strong longitudinal compression in the left low lateral cortex and strong longitudinal tensile stress in the right lateral cortex;
5. Moderately strong tensile stress in the greater trochanter, roughly aligned with abductor traction;
6. Moderate transverse compression in the neck-trochanter junction.

Further, we can see that those principal stress patterns correlate well with bony architecture. Detailed age-wise parametric variations of stress levels across the positions of interest, i.e., the load resultant line, are presented in Fig. 15. Longitudinal stresses and shear stresses along the line of the resultant joint force generally increased with age, see Fig. 15b and c. The increments of the values of the transverse stresses and the principal stresses with age across those positions are also observed, whilst a strong tendency toward distal concentration (between Positions 2 and 4) in these two kinds of stresses is observed, beginning after age seven. Part of this trend towards distal concentration is of course due to the fact that the load resultant line changes with age as femur neck-shaft angles progressively decrease.

6 Conclusions

In this study, a meshless methodology has been employed for the simulation of bone mechanics. The advantages of the meshless method over the finite element method are that it overcomes the difficulties associated with various element distortions such as the effects of skews and solid angle distortion and it also avoids the need for remeshing. Also, through treatment methods for nonconvex problems and material discontinuities, the bimaterial interface characteristics and complex geometries can be computed accurately. Numerical experiments of stress analysis for the proximal femur considering infarct and natural age effects were carried out. Results show that the present meshless method is an effective tool for the modeling the biomechanics. Some qualitative biome-

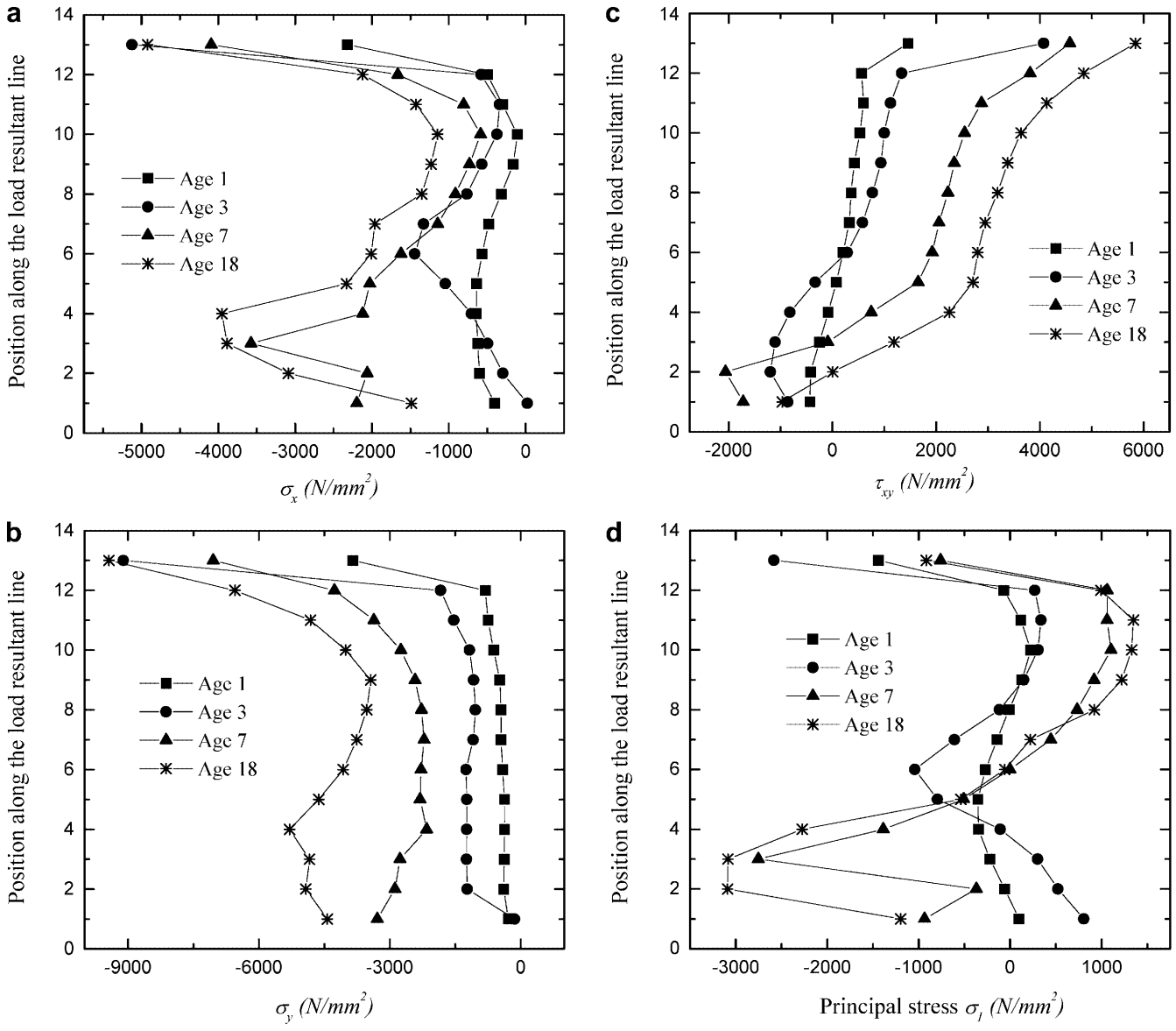

Fig. 15. The effects of age upon stress variations along the load resultant line: **a** normal stress σ_x; **b** normal stress σ_y; **c** shear stress τ_{xy}; **d** principal stress σ_1

chanical conclusions have been drawn from this analysis, which are in good general agreement with those reported by the previous studies. Since meshless methods are more appealing for dealing with large deformation problems, moving discontinuities, complex mesh and adaptivity problems, due to their unique meshless or gridless characteristic, a characteristic that traditional FEM inherently lacks, there holds greater promise for this tool, especially in the more complex biomechanics applications.

References

Belytschko T, Lu YY, Gu L (1994) Element-free-Galerkin methods. Int. J. Numer. Meth. Eng. 37: 229–256

Brown TD, Way ME, Fu FH, Ferguson Jr B (1982) Some femoral head load transmission changes occurring with infarction and with normal growth. Finite Ele. Biomech. 13: 269–294

Cordes LW, Moran B (1996) Treatment of material discontinuity in the element-free Galerkin method. Comp. Meth. Appl. Mech. Eng. 139: 75–89

Hansen TM, Koeneman JB (1987) The use of structural partitioning within ANSYS to solve non-linearities within human hip replacement models. Proc. of the 1987 ANSYS Conf. and Exhibition, Singapore

Hayes WC, Snyder B (1981) Toward a quantitative formulation of Wolff's law in trabecular bone. Mechanical Properties of Bone, ASME 120: 1–10

Hedia HS, Barton DC, Fisher J (1996) Effect of FE idealization, load conditions and interface assumptions on the stress distribution and fatigue notch factor in the human femur with an endoprosthesis. Bio-Medical Mat. Eng. 6: 135–152

Huiskes R, Chao ESY (1983) A survey of finite element analysis in orthopaedic biomechanics: the first decade. J. Biomech. 16: 364–375

Li S, Hao W, Liu WK (2000) Numerical simulations of large deformation of thin shell structures using meshfree methods. Comput. Mech. 25: 102–116

Liew KM, Ng TY, Wu YC (2002a) Meshfree method for large deformation analysis – a reproducing kernel particle method. Eng. Struct. 24 (in press)

Liew KM, Wu YC, Zou GP, Ng TY (2002b) Elasto-plasticity revisited: numerical analysis via reproducing kernel particle method and parametric quadratic programming. Int. J. Numer. Meth. Eng. (in press)

Liew KM, Ng TY, Zhao X, Reddy JN (2002c) Harmonic reproducing kernel particle method for free vibration analysis of rotating cylindrical shells. Comp. Meth. Appl. Mech. Eng. (in press)

Liu WK, Jun S, Li S, Adee JS, Belytschko T (1995a) Reproducing kernel particle methods for structural dynamics. Int. J. Numer. Meth. Eng. 38: 1655–1679

Liu WK, Jun S, Zhang YF (1995b) Reproducing kernel particle methods. Int. J. Numer. Meth. Fluids 20: 1081–1106

Organ D, Fleming M, Belytschko T (1996) Continuous meshless approximations for nonconvex bodies by diffraction and transparency. Comput. Mech. 18: 225–235

Sadegh AM, Luo GM, Cowin SC (1993) Bone in growth; an application of the boundary element method to bone remodeling at the implant interface. J. Biomech. 16: 141–169

Vander Sloten J, Labey L, Van Audekercke R, van der Perre G (1993) The development of a physiological hip prosthesis: evaluation of the strains after implantation of a prototype of hip implant: experiment in a dry femur. Bio-Medical Mat. Eng. 3: 1–13

Weinans H (1991) Mechanically induced bone adaptations around orthopaedic implants. PhD thesis, Katholieke Universiteit Nijmegen, Chs. 2 and 5

Yang RJ, Choi KK, Crowninshield RD, Brand RA (1984) Design sensitivity analysis, a new method for implant design and a comparison with parametric finite analysis. J. Biomech. 17: 849–854